buildings

MDPI

Article

Multiscale Numerical Analysis of TRM-Reinforced Masonry under Diagonal Compression Tests

Pietro Gulinelli [1,2,3,*], Alessandra Aprile [1], Raffaella Rizzoni [1], Yves-Henri Grunevald [2,3] and Frédéric Lebon [2]

[1] Department of Engineering, University of Ferrara, Via Saragat 1, 44122 Ferrara, Italy; alessandra.aprile@unife.it (A.A.); raffaella.rizzoni@unife.it (R.R.)
[2] Centre Nationale de la Recherche Scientifique (CNRS), Centrale Marseille, Laboratoire de Mecanique et Acoustique (LMA), Aix-Marseille Université, 4 Impasse Nikola Tesla, 13013 Marseille, France; yh.grunevald@composites-expertise-solutions.com (Y.-H.G.); lebon@lma.cnrs-mrs.fr (F.L.)
[3] Composites Expertise & Solutions, 131 Traverse Penne aux Camoins, BT 4 ID Dom Actiparc 1, 13821 La Penne-sur-Huveaune, France
* Correspondence: pietro.gulinelli@unife.it

Received: 23 September 2020; Accepted: 26 October 2020; Published: 31 October 2020

Abstract: The present paper reports an experimental study coupled with a numerical modelling approach to simulate masonry walls strengthened with textile-reinforced mortar (TRM). This innovative reinforcing technique is based on high-strength fibre grids embedded into inorganic matrices, and it has recently been promoted for the seismic retrofitting of historical masonry buildings. In the experimental campaign presented here, two different commercial TRM systems are applied to single-leaf clay masonry panels. The specimens are then subjected to diagonal compression tests in order to evaluate the effects of TRM on the structural performance. The proposed finite element (FE) model, based on an original multiscale approach, is employed to simulate the diagonal compression tests. The numerical results show a very good agreement with the experimental data, including in terms of failure mode. In particular, the approach reproduces the macroscopic behaviour of the masonry panels as regards the force-displacement response, and it allows for the possibility of simulating bed joint sliding and TRM layer debonding.

Keywords: strengthening masonry; diagonal compression test; numerical analysis; interface transmission conditions; cohesive law

1. Introduction

Historical structures made of solid brick or stone unreinforced masonry (UM) are widespread in Southern Europe and around the Mediterranean area, where a high earthquake hazard is concentrated. A majority of these UM buildings, located in regions of high seismic risk and mainly designed to resist gravity loads without special regard for lateral seismic forces, are nowadays in need of structural rehabilitation that takes into account their architectural and cultural value. A suitable procedure to select buildings needing structural rehabilitation is out of the scope of the present paper. The authors believe that the proposed numerical approach will be a useful tool for retrofit intervention design [1,2]. Jacketing historical masonry structures with steel-reinforced concrete is among the most conventional techniques for seismic retrofitting. The most recent improvements regarding materials and methods for structural reinforcement have highlighted the use of textile-reinforced mortar (TRM), also known as fibre-reinforced cementitious matrix (FRCM). TRMs are recently developed composite materials based on high-strength fibre (basalt, glass, steel) nets inserted into matrices made of natural mortars or cements. Many experimental studies have been conducted over the last decade to investigate

the effectiveness of TRMs in different load configurations. These works focus on TRM behaviour under in-plane load [3–18] and out-of-plane load conditions [9,12,19] and on the characterisation of the reinforcement–masonry bond for different typologies of fibres and mortars [10,20,21]. Experimental evidence shows that a relevant increase in strength, a better post-peak response and an evident increase in wall ductility can be achieved, especially when the TRM reinforcement is applied on both sides of the masonry panels. The latter effect typically contributes to the overall structural ductility when a global behaviour of the reinforced building is ensured [22]. However, some data indicate that failure may occur prematurely after loss of adhesion between the strengthening layer and the masonry substrate [6]. Various approaches have been proposed to quantify the strength of masonry walls externally reinforced with TRM techniques [6,10]. A review of TRM strengthening design and assessment procedures for in-plane and out-of-plane loading is provided in [23]. The effectiveness of classical design methods established for reinforced concrete beams and applied to TRM-reinforced masonry is discussed in [24], in view of some experimental data. In [6], the proposal of Faella et al., sourced from the scientific literature, juxtaposes documented shear strength relationships with experimental failure loads. These comparisons show the risk of considerable overestimation of the shear strength in models that are based on the reinforcement's ultimate tensile strength but neglect the premature loss of adhesion between the reinforcing layer and the masonry substrate. Finite element (FE) modelling of TRM-strengthened masonry is very useful for evaluating the influence of material constants on the reinforced structure's behaviour. In the technical literature, applications of numerical analysis have been mainly focused on simulations of the tensile response [25] and of bond behaviour [26–30]. However, investigations into the structural performances of TRM-strengthened masonry have been proposed with a limited number of numerical models [3,5,7,19,31–35]. In [3,31], an FE analysis is carried out using the computer code MIDAS-FEA and is based on a macroscopic nonlinear material model of masonry. The reinforcement is modelled using two layers of continuum isotropic materials, the textile and the matrix, perfectly bonded to the masonry substrate. In [5,34], numerical simulations are conducted in Ansys. In [5], masonry and mortar jackets are modelled separately, using three-dimensional elements. The internal reinforcement grid is discretised through three-dimensional spar elements embedded in the mortar mesh. Nonlinear constitutive laws are adopted for masonry and mortar jackets. Moreover, full displacement compatibility between the mortar jacketing and the internal grid prevents bond slippage. The approach proposed in [34] is based on similar assumptions; however, the strengthening layer is modelled with two-dimensional shell elements. In [19,32,33,35], numerical analyses are performed using the commercial FE package DIANA. The masonry wall is modelled as an equivalent homogeneous material in which the mechanical characteristics of mortar joints and masonry units are smeared. A perfect bond is adopted between the reinforcement and masonry panel as well as at the matrix–fibre interface. Notably, in all the cited works, the masonry is treated as an equivalent homogeneous material and the masonry substrate is put in perfect contact with the external reinforcement. In this paper, we propose an original multiscale approach for simulating the failure of TRM-reinforced masonry. The main feature of our approach is the introduction of cohesive contact laws at a microscopic scale, i.e., between masonry bricks and mortar joints and between reinforcement layers and wall substrate, through three-dimensional cohesive elements. These elements allow for the possibility of mortar joint sliding and reinforcement debonding, two occurrences frequently reported in the experimental literature. Bricks are modelled through continuum three-dimensional elements, made of homogeneous, isotropic and infinitely elastic material. Strengthening layers are described as homogenised laminates of equivalent material properties, discretised via two-dimensional elements. This new methodology, implemented in Abaqus, is used to predict the behaviour of masonry walls strengthened with two commercial TRM techniques in diagonal compression tests. Lastly, the proposed numerical model is tested on the original experimental results (cf. [36]). The present paper contains a complete description of the numerical model developed to simulate the TRM systems. A comparison with the experimental curves is another original contribution of this work. The remainder of the paper is structured as follows. An overview of the experimental campaign is presented in Section 2.

Here, together with the description and the results of the diagonal compression tests, we report on the mechanical characterisation of materials and mortar–brick interfaces. Section 3 presents an original model of the triplet tests classically used to characterise mortar–brick interfaces; the latter are simulated through FE analysis in order to derive the parameters of bond cohesion required to implement the numerical model. Section 4 is devoted to the numerical model's hypotheses in terms of FE discretisation, constitutive behaviour of cohesive elements, and assumed material properties. Section 5 describes the simulations of the diagonal compression tests and their comparison with the experimentally observed load-displacement macroscopic responses and damage behaviour. Finally, the conclusions are given in Section 6.

2. Experimental Campaign

The experimental investigation, fully conducted at LiFE S.r.l. (Ferrara, Italy), concerned in-plane diagonal compression tests on TRM-reinforced masonry panels as well as the mechanical characterisation of the materials (cf. [36]).

2.1. Building and Strengthening of Masonry Panels

The diagonal compression tests were conducted on 5 single-leaf masonry walls, 1030 mm^3 high, 1000 mm^3 wide and 120 mm^3 thick, characterised by 14 rows of clay bricks (CB) of average size $250 \times 55 \times 120$ mm^3, as illustrated in Figure 1.

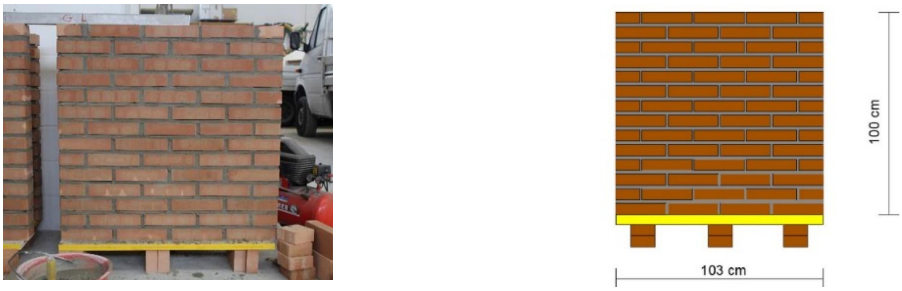

(**a**) (**b**)

Figure 1. (**a**) Masonry panel texture, (**b**) panel geometry.

A low-quality lime-based mortar (LM), made of sand (75%), lime (21%) and cement (4%), was used to realise bed joints (17 mm thick) and head joints (10 mm thick). Specimens were built and cured outdoor for 28 days (cf. [37]).

After this curing period, four of the five realised panels were strengthened using two commercial TRM systems with double-sided configuration. The first TRM system, denoted GTRM (Figure 2a) and applied to two specimens, consisted of preformed glass fiber-reinforced polymer (GFRP) grids (GG) inserted into a matrix of natural hydraulic lime mortar (GM).

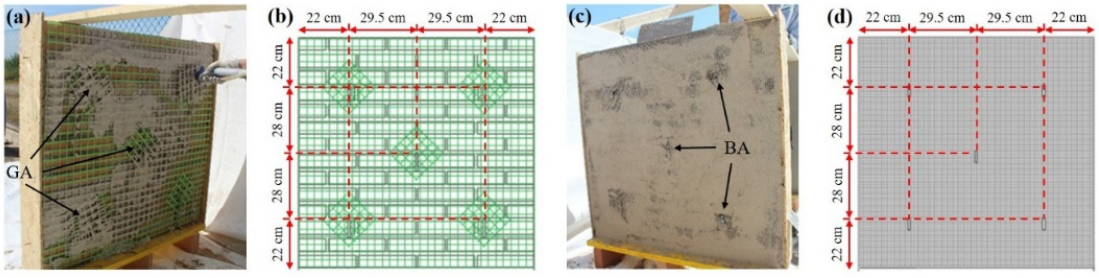

Figure 2. Strengthening systems: (**a**) GTRM; (**b**) GA configuration; (**c**) BTRM; (**d**) BA configuration.

Five GFRP anchors (GA), whose configuration is shown in Figure 2b, connected the two sides of the GTRM panels. The second TRM system, denoted BTRM (Figure 2c) and applied to two specimens, was based on balanced basalt–stainless steel grids (BG) embedded in a matrix of natural mineral binder-added lime mortar (BM). Five helical anchors of stainless steel (BA), whose configuration is shown in Figure 2d, connected the two sides of the BTRM panels.

Table 1 reports a description of the employed materials and the application methods provided by the manufacturers and followed in the preparation of the TRM layers.

Table 1. Strengthening configurations of the specimens.

Sample ID	Number of Samples	Matrix	Grid	Anchors
UM	1	—	—	—
GTRM	2	Hydraulic lime mortar (GM) sprayed in a single layer 30 mm thick on each side	Preformed GFRP square grid (GG), average thickness 3 mm, spacing 33×33 mm^2 each side	Coupled L-shaped preformed GFRP anchors (GA) of 70 mm^2 section, 100 mm long each
BTRM	2	Mineral binder-added lime mortar (BM) sprayed in two layers 10 mm thick each side	Balanced basalt–stainless steel AISI 304 square grid (BG), average thickness 0.064 mm, spacing 8×8 mm^2 each side	Helical stainless steel AISI 316 anchors (BA) of 14.5 mm^2 section, 200 mm long each

As specified by the manufacturers, the curing period of the TRM layers was 28 days. The last unreinforced panel (UM) was employed as a control specimen.

2.2. Mechanical Characterisation of Materials

Experimental tests for the mechanical characterisation of materials were conducted after a curing period of 28 days and followed standard approaches, even though numerous testing methodologies are available in the masonry component literature [38,39]. The tests are described in Table 2 by type, specimens, tested materials and derived mechanical properties.

Table 2. Description of the experimental tests for mechanical characterisation of materials.

Test Type	Standard Reference	Specimen Description	Materials ID	Corresponding Symbols
Compression	UNI EN 772-1, 2015 [40]	Cubes $40 \times 40 \times 40$ mm^3	CB, LM, GM, BM	f_c
Three-point bending	UNI EN 1015-11, 2007 [41]	Prisms $160 \times 40 \times 40$ mm^3	LM, GM, BM	f_t
Uniaxial compression	EN 1052-1, 2001 [42]	Single-leaf wall $645 \times 630 \times 120$ mm^3 (bricks: $250 \times 55 \times 120$ mm^3)	CB + LM	E, ν

The results of mean values and coefficients of variation (CV) are reported in Table 3.

Table 3. Experimentally measured mechanical properties of materials.

	Bending Tests			Compression Tests				
Material ID	**Number of Samples**	**f_t (N/mm^2)**	**CV (%)**	**Number of Samples**	**f_c (N/mm^2)**	**CV (%)**	**E (N/mm^2)**	**ν**
CB	—	—	—	20	19.37	12	20176	0.23
LM	18	0.84	25	36	4.64	15	2499	—
GM	3	1.14	10	6	4.58	5	—	—
BM	3	2.05	17	6	8.16	3	—	—

The grids' and anchors' mechanical properties were provided by the manufacturers (Table 4).

Table 4. Geometrical and mechanical properties of grids and anchors as provided by manufacturers.

Material ID	Tensile Strength (N/mm^2)	Elastic Modulus (N/mm^2)	Ultimate Strain (%)
GG	≥350	≥27	≥1.5
BG	≥1700	≥70	≥1.9
GA	≥440	≥26	≥1.7
BA	≥700 (ε = 0.2%)	≥150	≥3.0

As seen from Tables 2 and 3, GM and BM elastic constants were not investigated during the materials' characterisation. However, these parameters were required for implementing our numerical model. For GM, the manufacturer's dataset only provided an upper limit of 8000 N/mm^2 for the compression modulus. For the purpose of our numerical analysis, the GM elastic modulus was estimated using the following relationship (cf. [43]), Equation (1):

$$E_c = k_c\left(\frac{f_c}{10}\right)^{0.3} \quad (1)$$

which is used to link the compression modulus E_c to the compression strength f_c. Equation (1) can also be empirically applied to mortars, as suggested in [44]. For the mortars used in our TRM application, the coefficient k_c can be estimated as equal to 3146, by using E_c and f_c measured for LM (cf. Table 3). Substituting this value and the f_c of GM into Equation (1), the compression elastic modulus E_c of GM was estimated as equal to 2489 N/mm^2. Poisson's ratios for LM, GM and BM were assumed to be the same and all equal to 0.15. The assumed values of E and ν for LM, GM and BM are summarised in Table 5.

Table 5. Assumed elastic constants of the used mortars.

Material ID	k_c	E (N/mm^2)	N
LM	—	2499	0.15
GM	3146	2489	0.15
BM	—	9000	0.15

2.3. Characterisation of Mortar–Brick Interfaces

The initial shear strength of the mortar–brick interfaces, f_{v0}, was estimated by using triplet tests, according to the standard UNI EN 1052-3 (2007) [45]. The main results are summarised in Table 6 in terms of mean values and coefficients of variation (CV).

Table 6. Bond strength of mortar–brick and matrix–brick interfaces.

Interface ID	Number of Samples	f_{v0} (N/mm^2)	CV (%)
CB-LM	8	0.29	23
CB-GM	3	0.36	36
CB-BM	3	0.37	68

The CB-BM system is characterised by a high CV (cf. Table 6). A similar dispersion of values was found in [46]. The standard UNI EN 1052-3 (2007) [45] provides a list of possible failure modes: triplet crush, mortar joint shear cracking, brick shear cracking and debonding at the mortar–brick interface. However, the most observed failure mode was debonding. The observed fracture modes are shown in Figure 3.

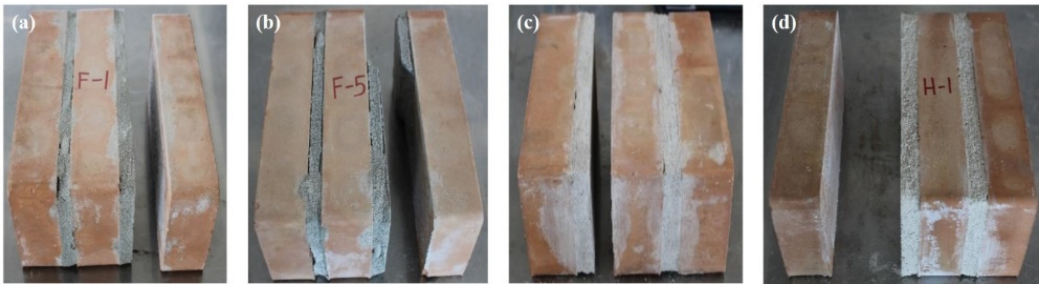

Figure 3. Observed triplet failure modes: (**a**) CB-LM 7/8; (**b**) CB-LM 1/8; (**c**) CB-GM 3/3; (**d**) CB-BM 3/3.

For the CB-LM system, seven of the eight tested specimens debonded at the inteface between mortar and exterior bricks (Figure 3a), while just one triplet exhibited a crack along the mortar joint (Figure 3b). All CB-GM specimens failed for debonding at the interface between mortar and interior brick (Figure 3c). Finally, all CB-BM triplets (Figure 3d) showed the same fracture mode as that observed for CB-LM specimens in Figure 3a. Since interface debonding was the predominant fracture mode, the measured shear strength f_{v0} can be assumed as the mortar–brick interface bond shear strength.

2.4. In-Plane Diagonal Compression Tests

Diagonal compression tests were conducted on UM, GTRM and BTRM panels, conforming to the standard ASTM E519 (2007) [47]. According to the test set-up schematisation in Figure 4a, a servo hydraulic system with an electrical pump applied the diagonal compression load.

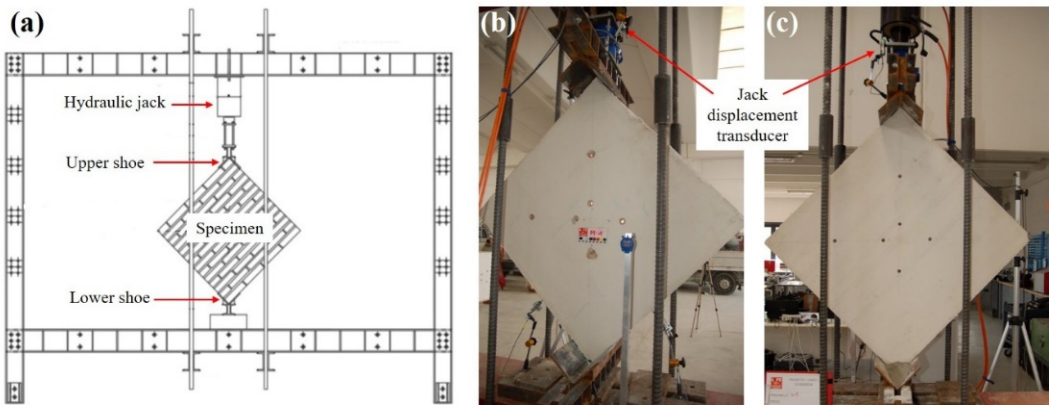

Figure 4. (**a**) Test set-up schematisation; (**b**) specimen GTRM-1 and (**c**) specimen BTRM-1 in the testing device.

The load was transmitted to the specimen corners through two steel shoes (upper shoe and lower shoe, Figure 4a). A thin layer of shrinkage-free mortar was interposed between the steel shoes and the masonry panel to prevent local brittle fractures at the contact surface. The tests were carried out under displacement control, with a deformation rate of 0.08 mm/s. The vertical in-plane displacement was monitored by a displacement transducer interposed between jack head and upper shoe, as shown in Figure 4b,c for the specimens GTRM-1 and BTRM-1, respectively. The monitored displacement corresponds to the relative displacement between upper and lower corners on the vertical diagonal.

The main experimental results in terms of peak loads (P_p), vertical peak displacements (δ_p), their relative average values and failure modes are summarised in Table 7.

Table 7. Experimental results: peak loads, peak deformations and failure modes.

Specimen ID	P_p (kN)	$P_{p,av}$ (kN)	$\Delta P_{p,TRM/UM}$ (%)	δ_p (mm)	$\delta_{p,av}$ (mm)	$\Delta\delta_{p,TRM/UM}$ (%)	Failure Mode
UM	71	71	—	0.28	0.28	—	Bed joint sliding
GTRM-1 GTRM-2	146 162	154	+117	0.65 0.78	0.72	+157	TRM debonding
BTRM-1 BTRM-2	198 167	183	+158	0.35 0.31	0.33	+18	Diagonal traction

According to these results, both strengthening solutions exhibited an important increase in the average load carrying capacity: +117% for GTRM and +158% for BTRM. Nevertheless, GTRM presented a meaningful gain in the average peak displacement (+157%), unlike BTRM for which $\delta_{p,av}$ increased only slightly (+18%).

The relationships between vertical displacement (δ) and vertical load (P) obtained from the tests are reported in Figure 5, while the observed failure modes are shown in Figure 6.

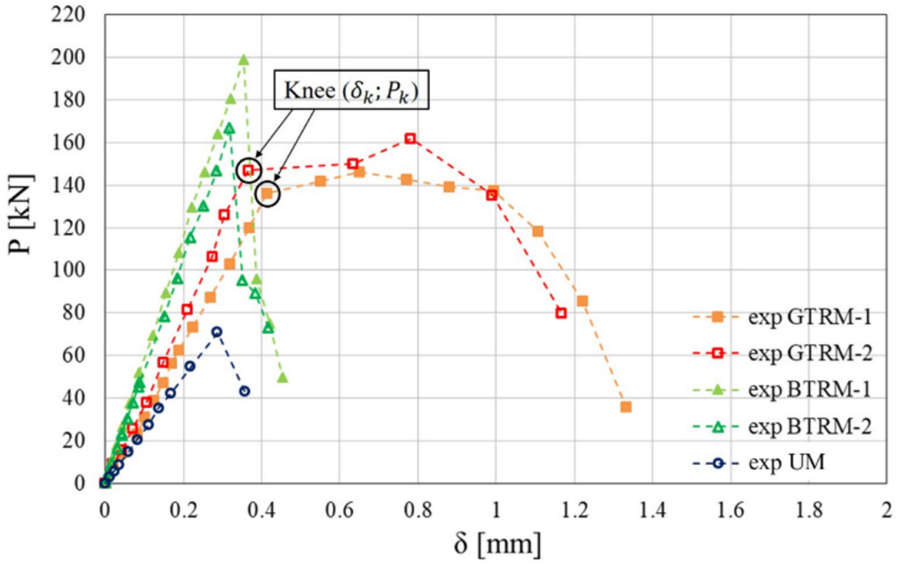

Figure 5. Experimental results: vertical load (P) vs vertical displacement (δ).

Figure 6. Failure modes observed in (**a**) UM, (**b**) GTRM, (**d**) BTRM and (**c**) GTRM debonding detail.

The UM specimen presented an essentially linear elastic behaviour and a brittle fracture caused by bond sliding at the upper 5th bed joint (Figure 6a). A similar behaviour was observed by Wang et al. in [15]. Following the schematisation proposed in [15], GTRM curves can be divided into two parts: an initial linear part, followed by a knee and a subsequent nonlinear part. The knee point (Figure 5) is defined by P_k and δ_k (cf. Table 8).

Table 8. Experimental results: knee loads, knee displacements and estimated stiffness results.

Sample ID	P_k (kN)	$P_{k,av}$ (kN)	δ_k (mm)	$\delta_{k,av}$ (mm)	K (kN/mm)	K_{av} (kN/mm)	$\Delta K_{TRM/UM}$ (%)
UM	—	—	—	0.28	243	243	—
GTRM-1	136	142	0.41	0.39	332	365	+50
GTRM-2	147		0.37		397		
BTRM-1	—	—	—	—	566	553	+128

This point is classically associated with the initiation of a crack in the bare wall [15], followed by an abrupt decrease in stiffness. In the nonlinear part, the load keeps increasing while the reinforcement debonds from the wall surface (Figure 6b). When the peak load is reached, bed joint sliding causes the ultimate failure (Figure 6c). Moreover, it can be noticed that the GTRM-1 specimen exhibited a smoother post-peak behaviour than GTRM-2. Finally, BTRM specimens presented a pre-peak linear elastic behaviour and exhibited a typical diagonal failure immediately after the peak force, due to traction in the horizontal direction. Due to these observed trends (Figure 5), P_k and δ_k have not been defined for BTRM specimens (cf. Table 8). As shown in Figure 6d, diagonal cracks were observed both in bricks and in the TRM layer matrix, demonstrating the reinforcement's high efficiency.

Table 8 reports the estimated pre-peak stiffnesses (K) and their relative average values. For UM and BTRM, the stiffness K is calculated using P_p and δ_p (Table 7), while for GTRM it is estimated using P_k and δ_k. An important increase in average stiffness can be noticed for both strengthening systems, especially for BTRM (+128%).

3. Numerical Investigation of Interface Properties

Interface bond cohesion (c_b), defined as the interface bond shear strength at zero normal stress, is an important requested parameter for the implementation of the numerical model. According to the standard UNI EN 1052-3 (2007) [45], the average shear stress measured in triplet tests to estimate the interface bond strength of a single specimen is calculated using Equation (2):

$$f_{v0,i} = \frac{F_{max,i}}{2A_i} \quad (2)$$

where $F_{max,i}$ is the maximum shear load and A_i the specimen's transversal area parallel to the mortar joint. The average bond strengths for the three tested brick–mortar interfaces are listed in Table 6. It is

believed that f_{v0} is affected by non-zero normal stress distribution and thus cannot be considered as providing a realistic estimate of the interface bond cohesion. To provide a more realistic estimation of c_b, we adopted the following original strategy. The triplet shear test was modelled in Abaqus for each of the three used mortars (LM, GM and BM), according to the standardised configuration, cf. UNI EN 1052-3 (2007) [45]. All materials are considered isotropic and infinitely elastic, and perfect contact was assumed between bricks and mortar. A thin layer of mortar elements, hereafter denoted as IL (interface layer), was used to represent the mortar–brick interface where debonding was experimentally observed, i.e., the fracture surface (Figure 3a,c,d). During the simulation, we monitored the numerical average shear stress in the IL. The simulation was stopped when the monitored shear stress equalled the measured bond strength f_{v0} of the studied mortar (cf. Table 6). This allows an analysis of the numerical normal stress and shear stress distributions in the IL at the instant of debonding. Finally, a new c_b estimate is obtained with an iterative analytical procedure based on the Mohr–Coulomb failure criterion [48,49], as a function of the numerical normal and shear stresses in the IL.

3.1. Triplet Numerical Model and Shear Test Simulation

Figure 7a shows the model set-up and the boundary conditions for the CB-LM triplet. Clay bricks (CB) were discretised through continuum three-dimensional elements (C3D8R), with a side average size of 10 mm.

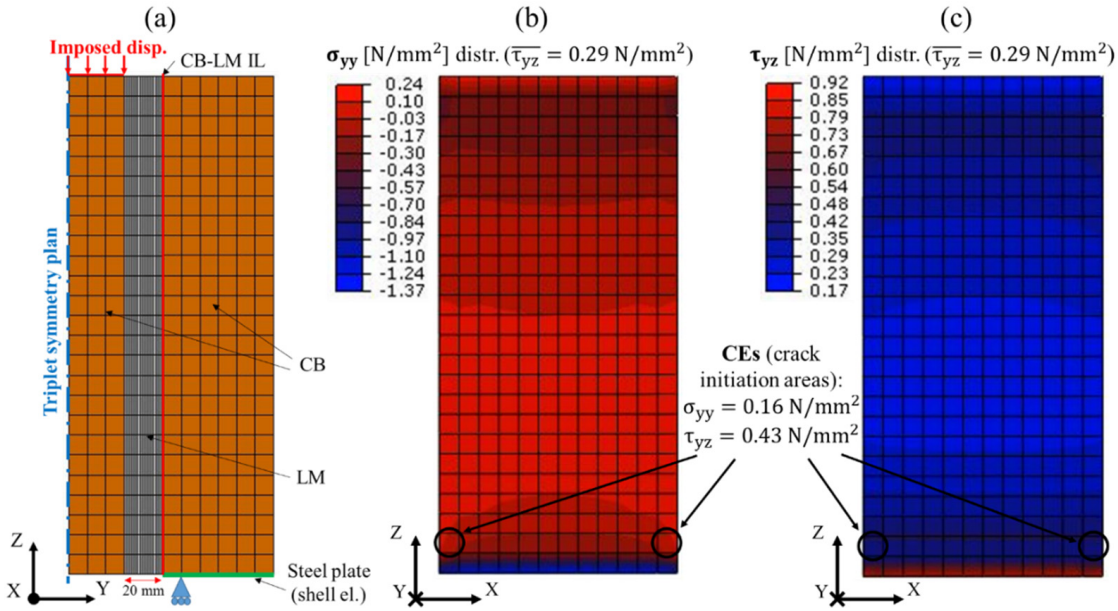

Figure 7. (**a**) Triplet model set-up; (**b**) normal stress and (**c**) shear stress distributions in the CB-LM IL for $\overline{\tau_{yz}} = f_{v0}$.

The same element type was used to model LM. Moreover, LM was divided into 20 layers, each 1 mm thick (20 mm of total thickness), in which the one bonded to the exterior brick in Figure 7a (red layer) represents the CB-LM IL. At exactly this last layer, a fracture surface was observed in most (seven out of eight) of the CB-LM triplets tested during the experimental campaign (Figure 3a). The elastic constants of CB and LM are reported in Tables 3 and 5, respectively. Finally, the steel plate (Figure 7a), required in [45], was modelled with 5 mm thick shell elements (S4R), assumed to be in perfect contact with the lower surface of the exterior brick. To reproduce the shear test, a vertical displacement was imposed on the top nodes of the central brick (Figure 7a) in static conditions. A preliminary mesh sensitivity analysis suggested that, during the simulation, there was no occurrence of distorsion problems due to the high side-to-thickness ratio of mortar elements.

Figure 7b,c shows normal stress σ_{yy} and shear stress τ_{yz} distributions in the CB-LM IL, where positive values of σ_{yy} denote tensile stress. As stated above, these stress distributions are observed when $\overline{\tau_{yz}}$ (i.e., the average τ_{yz} in the IL) is equal to f_{v0} (0.29 N/mm^2 for the interface CB-LM, cf. Table 6). It can be seen that the distribution of τ_{yz} (Figure 7c) is not uniform and there is also a non-zero normal stress contribution (σ_{yy}, Figure 7b).

3.2. Analytical Procedure to Estimate c_b

Given the brittle nature of the materials used, it can be assumed that the crack, after initiation, propagates instantaneously on the overall fracture surface. In our model, the fracture surface is modelled by the IL. We suppose that there are some elements of the IL, denoted as CEs (critical elements), that correspond to the real crack initiation areas, and we approximate c_b as the bond cohesion estimated for these areas. The following procedure applies the Mohr–Coulomb failure criterion to locate the CEs in order to obtain an estimation for c_b. Before illustrating the procedure, some assumptions must be made. According to the Mohr–Coulomb failure criterion [48,49], the bond strength τ_{yz}^c (the superscript c indicates damage initiation) generally depends on normal stress σ_{yy} as follows, Equations (3) and (4):

$$\tau_{yz}^c = c_b - \mu\sigma_{yy} \tag{3}$$

$$\mu = \frac{c_b}{\sigma_{yy}^c} = \frac{c_b}{f_t} \tag{4}$$

where μ is the Coulomb friction coefficient. The critical normal stress in traction σ_{yy}^c in Equation (4) is assumed to be equal to the average mortar bending strength f_t (Table 3). The friction contribution was not investigated during the experimental campaign because the triplet bending tests were not conducted with increasing pressures. The procedure to estimate c_b is as follows. A critical ratio (CR) is introduced to locate the CEs of the CB-LM IL. Equation (5) expresses the critical ratio CR_i where the subscript i indicates the i^{th} generic element of the CB-LM IL (Figure 7a), characterised by its $\sigma_{yy,\,i}$ and $\tau_{yz,\,i}$.

$$CR_i = \frac{\tau_{yz,\,i} + \frac{c_b'}{f_t}\sigma_{yy,\,i}}{c_b'} \tag{5}$$

Equation (5) is obtained by replacing Equation (4) in Equation (3) and inverting Equation (3).

Here, the superscript $'$ indicates an attempted value, since the effective c_b is still unknown. The higher the value of CR_i, the more critical the ith element is. Moreover:

- If $CR_i < 1$, the area corresponding to the ith element is not a crack initiation site.
- If $CR_i = 1$, the ith element is a CE, i.e., cracking initiates in the corresponding area.
- If $CR_i > 1$, the corresponding area is assumed to be already fractured.

Since a crack propagates instantaneously after its initiation, c_b' corresponds to the effective c_b when the maximum CR_i is equal to 1. Figure 8 illustrates the iterative process to estimate c_b through Equation (5).

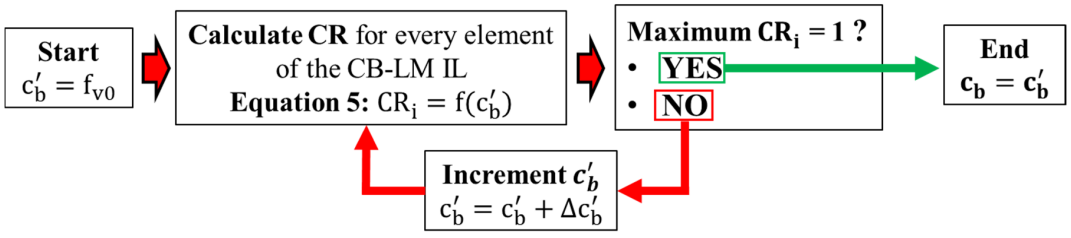

Figure 8. Iterative process to estimate bond cohesion.

For the first iteration ("Start" case in Figure 8), c_b' can be taken as equal to f_{v0} (Table 6). The increment $\Delta c_b'$ can be positive or negative, depending if the maximum CR_i is higher or lower than 1, respectively. Figure 7b,c shows the location of the CEs for CB-LM IL with their σ_{yy} and τ_{yz}. The corresponding c_b (0.53 N/mm^2) is reported in Table 9.

Table 9. Estimated interface bond cohesion.

Interface ID	c_b (N/mm^2)
CB-LM	0.53
CB-GM	0.64
CB-BM	0.88

The same procedure, based on FE simulation and c_b estimation, can be repeated for CB-GM and CB-BM triplets, according to the following important points:

- As done for CB-LM (Figure 7b,c) to analyse the IL in the instant of debonding, σ_{yy} and τ_{yz} distributions must be observed when $\overline{\tau_{yz}}$ is equal to f_{v0} of the corresponding triplet (Table 6).
- For the CB-GM system, the IL was assumed to be located between the interior brick and the mortar joint because of the experimental evidence (cf. Figure 3c).

For CB-GM IL and CB-BM IL, the CEs are approximately located in the same positions as for CB-LM IL. For the sake of brevity, we have not reported normal and shear stress distributions in the IL for the CB-GM and CB-BM systems. The estimated values of c_b are reported in Table 9. It can be noticed that each one is greater than the corresponding measured f_{v0} given in Table 6.

4. Numerical Model for the Diagonal Compression Test

The developed FE model was imported in Abaqus following a simplifying micro-model methodology [48,49]. The bare masonry wall is made of expanded units, each one embedding a brick plus the half thickness of the adjacent bed and head joints (Figure 9a, cf. Section 2.1 for mortar joint thickness).

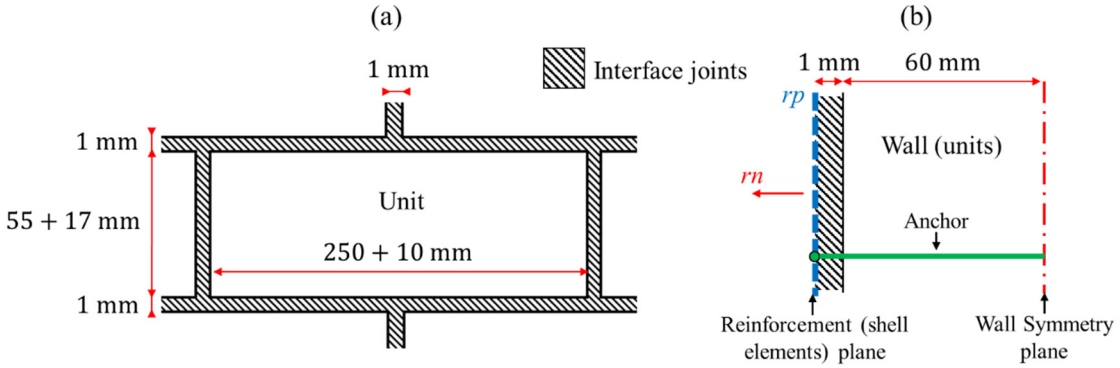

Figure 9. Modelling of (**a**) masonry wall and (**b**) wall–reinforcement interaction.

The wall units are modelled with continuum three-dimensional elements (C3D8), under the assumption of homogeneous, isotropic and infinitely elastic materials, whose brick elastic constants are given in Table 3. The units were bonded together by 1 mm thick interface joints (Figure 9a) discretised with three-dimensional cohesive elements (COH3D8), which were used to introduce damage in the masonry wall, and in particular the possibility of joint sliding and joint separation. With respect to reinforcement, TRM layers were implemented as composite laminates with homogenised elastic properties. They were discretised with two-dimensional shell elements (S4), positioned on the

reinforcement plane (*rp*) and with normal *rn* (Figure 9b). Section 4.1 provides more details about TRM layer modelling and properties. Once again, three-dimensional cohesive elements (COH3D8) were used in the 1 mm thick interface joints, which bonded TRM layers to the wall substrate (Figure 9b). These cohesive elements were employed to introduce damage at the TRM–wall interface and, in particular, to allow for TRM debonding. The constitutive behaviour of the cohesive elements is described in Section 4.2.

Finally, one-dimensional elements discretise the anchors of the strengthening system (Figure 9b). More details are reported in Section 4.3.

4.1. Reinforcement Layer Modelling

Composite stacking for glass-based and basalt-based TRMs (Figure 10) was assumed according to their respective construction techniques (Table 1).

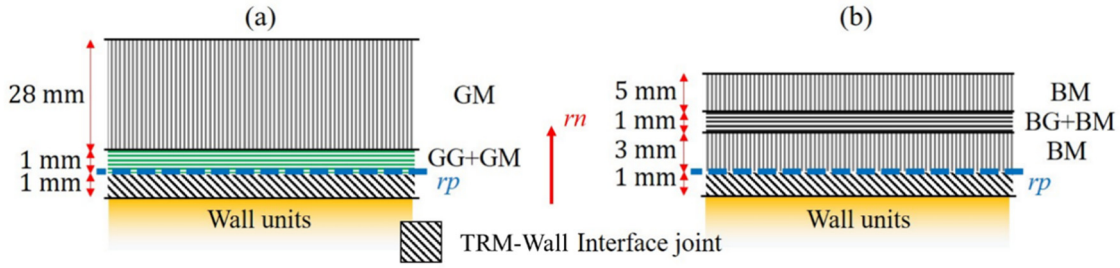

Figure 10. Assumed composite laminates: (**a**) glass-based TRM, (**b**) basalt-based TRM.

Summing the thicknesses of the laminate (Figure 10) and of the wall–TRM interface joint (1 mm, Figure 10), the real total TRM thickness was obtained.

All materials employed in composite laminates were assumed to be homogeneous and infinitely elastic. The matrices GM and BM are isotropic (Table 5). The grid/matrix plies (GG + GM, Figure 10a and BG + BM, Figure 10b) are assumed to have orthotropic symmetry with two orthotropic axes parallel to the fibres' directions, and equivalent thickness $h_{gm}^{eq} = 1$ mm. Equation (6) is used to obtain the equivalent fibre thickness h_f^{eq}, as a function of grid weight per surface unit γ_g, provided by the constructors, and fibre mass density ρ_f (Table 10):

$$h_f^{eq} = \frac{\gamma_g}{\rho_f} \tag{6}$$

Table 10. Grid mass and fibre density.

Material ID	$\gamma_g\ (g/m^2)$	$\rho_f\ (kg/m^3)$	$\rho_m\ (kg/m^3)$
GG	1000	2600	—
BG	400	2750	—
GM	—	—	1400
BM	—	—	1580

The fibre volume ratio V_f^{eq} of grid/mortar plies, Equation (7), enables the calculation of the homogenised density ρ_{gm} with the rule of mixtures expressed in Equation (8) (cf. [50]), as a function of fibre and mortar densities (ρ_f and ρ_m respectively, Table 10).

$$V_f^{eq} = \frac{h_f^{eq}}{h_{gm}^{eq}} \tag{7}$$

$$\rho_{gm} = V_f^{eq}\rho_f + \left(1 - V_f^{eq}\right)\rho_m \tag{8}$$

Grid/mortar plies are treated as bidirectional symmetric composite laminates [0°, 90°, 90°, 0°], in which each sub-ply is 0.25 mm thick. The rule of mixtures, similarly to Equation (8) for ρ_{gm}, and composite laminate theory are used to calculate their associated ABBD matrices [50] and to obtain grid/matrix plies' homogenised elastic constants on the *rp* plane (Figure 10) (cf. Table 11).

Table 11. Homogenised properties of the grid mortar/plies.

Ply	h_f^{eq} (mm)	V_f^{eq}	ρ_{gm} (kg/m^3)	E_{rp} (N/mm^2)	ν_{rp}	G_{rp} (N/mm^2)
GG + GM	0.384	0.384	1862	8464	0.12	2072
BG + BM	0.145	0.145	1750	14507	0.13	4863

The approximation of the symmetric laminate allows the deletion of coupling terms in ABBD matrices [50]. The homogenised elastic constants out of the *rp* plane are taken as equal to the corresponding mortar ones.

4.2. Constitutive Behaviour of Interface Joints

The constitutive model of the cohesive elements employed in the interface joints (Figure 9) assumes a traction-separation (**t-δ**) law, with **t** the traction vector and **δ** the relative opening. This contact law exhibits an initial linear elastic response, followed by damage softening [48,49], as depicted in Figure 11.

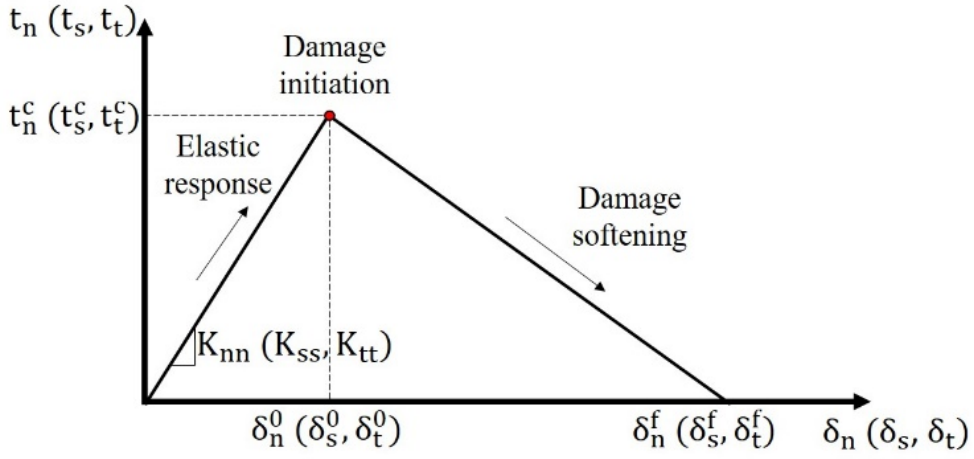

Figure 11. Interface joint traction-separation response in tension and shear.

Here, the subscripts s, t and n are taken to denote in-plane shear components and the out-of-plane normal component, respectively. Superscripts c and 0 are taken to denote damage initiation, while f denotes failure.

The cohesive behaviour takes into account two different failure modes at the contact surface: tensile cracking and shear sliding. According to the recent literature [48,51], Equation (9) [52] is used to describe the initial linear elastic part as a function of traction **t**, stiffness **K** and separation **δ**:

$$\mathbf{t} = \begin{pmatrix} t_n \\ t_s \\ t_t \end{pmatrix} = \begin{bmatrix} K_{nn} & 0 & 0 \\ 0 & K_{ss} & 0 \\ 0 & 0 & K_{tt} \end{bmatrix} \begin{pmatrix} \delta_n \\ \delta_s \\ \delta_t \end{pmatrix} = \mathbf{K}\boldsymbol{\delta} \quad (9)$$

The diagonal components (K_{nn}, K_{ss}, K_{tt}) depend on the elastic and shear moduli of the mortar (E_m and G_m, respectively). Many equations have been proposed in the literature for this

purpose [48,49,53,54]. In this study, the stiffness components are obtained through Equations (10) and (11) proposed in [54]:

$$K_{nn} = \frac{G_m(E_m - 4G_m)}{h_m(E_m - 3G_m)} \tag{10}$$

$$K_{ss} = K_{tt} = \frac{G_m}{h_m} \tag{11}$$

This interface model, appropriate for very thin layers, was adopted for its simplicity. For thicker layers, more complicated models should be used, considering higher order terms (cf. [55]). For bed and head joints, h_m represents the effective thickness; for the contact surface between TRM and the wall, h_m is the thickness of the cohesive element (1 mm, Figure 9), thus allowing an analysis of the two studied TRM techniques adopting the same mesh. Table 12 reports the elastic properties of the different interface joints.

Table 12. Parameters of interface joint materials.

Interface Joint	Mortar	h_m (mm)	K_{nn} (N/mm^3)	K_{ss} (K_{tt}) (N/mm^3)	t_n^c (N/mm^2)
Bed joint in UM	LM	17	149	61	0.84
Head joint in UM	LM	10	264	108	0.84
TRM–wall	GM	1	2640	1087	1.14
TRM–wall	BM	1	9503	3913	2.05

Damage propagation in the cohesive joints is taken into account in the post-peak phase. The maximum stress criterion (MAXS, Abaqus) was used to identify local damage initiation [52]. The damage initiation criterion is met when one of the three components of **t** reaches its critical value, Equation (12):

$$\max\left\{\frac{\langle t_n \rangle}{t_n^c}, \frac{t_s}{t_s^c}, \frac{t_t}{t_t^c}\right\} = 1 \tag{12}$$

where Macaulay brackets $\langle\ \rangle$ in Equation (12) indicate the positive part and imply that only tensile stresses participate in damage initiation to the joint's normal direction. The critical normal stress t_n^c is fixed and is assumed to be equal to the mortar bending strength f_t (Table 3). The values of t_n^c are also reported in Table 12 for the different cohesive joints. According to the Mohr–Coulomb failure criterion [48,49], critical shear stresses in Equation (12) (t_s^c and t_t^c) will depend on the normal stress t_n similarly to Equation (3), as expressed in Equation (13):

$$t_s^c = t_t^c = c_b - \mu t_n \tag{13}$$

where μ represents the Coulomb friction coefficient, already defined in Equation (4) as a function of c_b and f_t. The values of c_b and f_t are reported in Tables 3 and 9, respectively. A user subroutine USDFLD was developed to implement Equation (13) (cf. [52]). Damage propagation in the post-peak phase is taken into account as follows, Equation (14):

$$\mathbf{t} = (1 - D)\mathbf{K}\boldsymbol{\delta} \tag{14}$$

where D is a scalar damage variable increasing from 0 (damage initiation) to 1 (joint completely damaged) during damage softening (Figure 11). As suggested in [48,52], an effective opening δ_{eff} should be introduced, defined as follows, Equation (15):

$$\delta_{eff} = \sqrt{\langle \delta_n \rangle^2 + \delta_s{}^2 + \delta_t{}^2} \tag{15}$$

Because the goal is modelling the elastic response before damage initiation, the damaged response depends linearly on the effective separation δ_{eff}. Therefore, the only input for Abaqus

is $\delta_{eff}^{f} - \delta_{eff}^{0} = 0.1$ mm in the material description [52]. This value was chosen for all interface joints, according to [49]. The evolution of the damage variable D during damage is described in Equation (16) [56]:

$$D = \frac{\delta_{eff}^{f}\left(\delta_{eff}^{max} - \delta_{eff}^{0}\right)}{\delta_{eff}^{max}\left(\delta_{eff}^{f} - \delta_{eff}^{0}\right)} \quad (16)$$

where δ_{eff}^{max} is the maximum effective separation attained during the loading history, δ_{eff}^{0} the relative effective separation at joint damage initiation and δ_{eff}^{f} the final effective separation, when the joint is completely damaged.

4.3. Modelling of Anchors

Anchors were modelled through linear beam elements (B31), characterised by displacement compatibility with masonry wall nodes. Numerical anchors, made of isotropic, homogeneous and infinitely elastic material, are connected to the reinforcement layer in the *rp* plane by a node (Figure 9b). According to the manufacturer's specifications (Table 1), numerical GA represents a rectangular cross-section of 7×10 mm^2, while numerical BA is characterised by an equivalent circular cross-section of area 14.5 mm^2. Material properties, as provided by manufacturers, are listed in Table 4.

5. Results and Discussion

Figure 12a shows the bare wall surface of the realised numerical model, characterised by an average mesh size of 30 mm, as suggested by mesh sensitivity analysis.

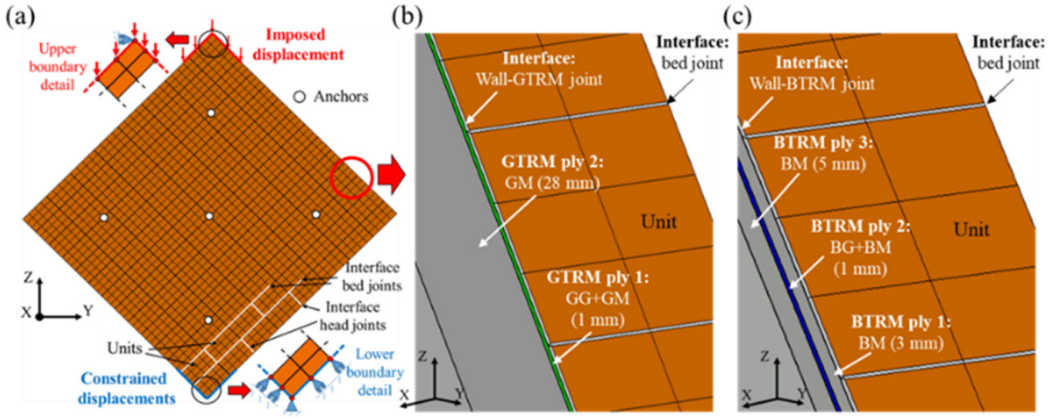

Figure 12. (**a**) Numerical model layout; representation of the (**b**) GTRM–wall and (**c**) BTRM–wall interactions.

Numerical anchors (round ticks, Figure 12a) are located according to the experimental configuration (Figure 2b,d). Figure 12a also shows the upper (in red) and lower (in blue) imposed boundary conditions, with a detail of the constrained nodes. The conditions applied to upper and lower vertices prevent displacement in the Y direction. The vertical displacement imposed on the upper nodes allows the transmission of the vertical load to the masonry panel during the simulation. In the lower part, the mobile pins allow the constrained nodes to move along the panel edges. For GTRM and BTRM, the same boundary conditions are also applied to the nodes of the TRM layers. The main general features of the simulation approach are as follows:

- symmetry plane YZ;
- FE analyses performed in a dynamic regime, in order to better deal with the nonlinearity of the constitutive cohesive law;
- imposed vertical displacements at the boundary (Figure 12a) in quasi-static conditions to simulate the low jack displacement rate of the experimental tests (0.08 mm/s).

A representation of wall–TRM laminate interactions is given in Figure 12b,c, for the GTRM and BTRM systems, respectively. Experimental and numerical results are further compared in terms of vertical load (P) and vertical displacement (δ).

Figure 13 shows the experimental and numerical P-δ curves.

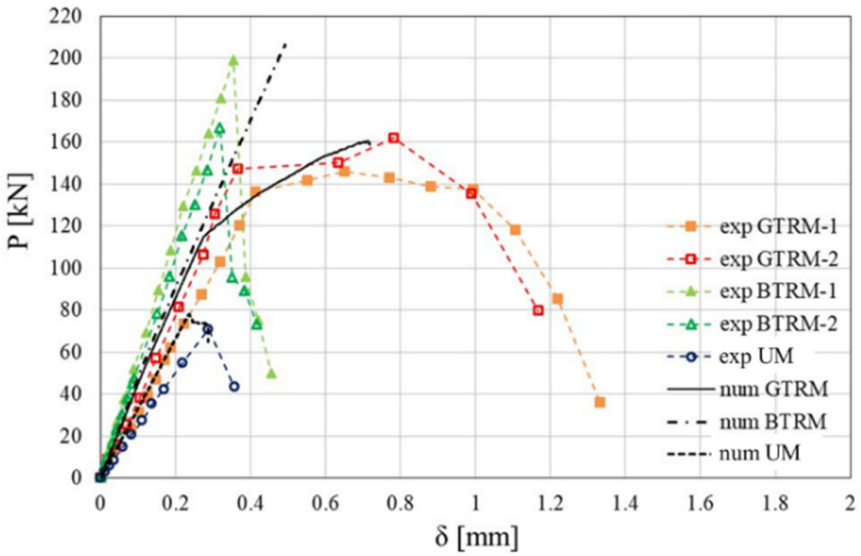

Figure 13. Comparison of experimental and numerical results: vertical load vs vertical displacement.

The experimental and numerical trends are in fairly good agreement, despite the absence of a post-peak softening phase for the GTRM and BTRM numerical curves. In particular, the numerical model is able to catch the two-fold trend of GTRM experimental curves, characterised by the knee point (P_k and δ_k) and also observed in [15]. The BTRM numerical curve ("num BTRM" in Figure 13) was obtained by assuming that no damage occurs in the bed and head interface joints (Figure 9a). Indeed, it was found that the numerical model omitted to reproduce the BTRM damage behaviour, showing an absence of bed joint sliding. With the assumption of neglecting bed and head joint sliding, the numerical BTRM linear elastic trend shown in Figure 13 predicts the experimental curve more accurately.

Table 13 summarises the numerical results in terms of peak loads, peak displacements, relative average values and failure modes, providing a comparison with the corresponding experimental values.

Table 13. Numerical results (peak load, peak displacement, failure mode) and comparison with the experimental values.

Specimen ID	$P_{p,num}$ (kN)	$P_{p,exp,av}$ (kN)	$\Delta P_{p,num/exp}$ (%)	$\delta_{p,num}$ (mm)	$\delta_{p,exp,av}$ (mm)	$\Delta\delta_{p,num/exp}$ (%)	Numerical Failure Mode
UM	78	71	+9	0.24	0.28	−14	Bed joint sliding
GTRM	161	154	+5	0.65	0.72	−10	TRM debonding
BTRM	206	183	+13	0.49	0.33	+48	TRM debonding

The average experimental peak loads are slightly overestimated by numerical predictions, with a maximum error of 13% for BTRM. A good numerical correlation can also be noticed for UM and GTRM average peak displacements, while a lower accuracy characterises the prediction of BTRM.

The numerical results for knee load, knee displacement, stiffness and relative average values are compared with the corresponding experimental values in Table 14.

Table 14. Numerical results (knee load, knee displacement, stiffness) and comparison with the experimental values.

Specimen ID	$P_{k,num}$ (kN)	$P_{k,exp,av}$ (kN)	$\Delta P_{k,num/exp}$ (%)	$\delta_{k,num}$ (mm)	$\delta_{k,exp,av}$ (mm)	$\Delta\delta_{k,num/exp}$ (%)	K_{num} (kN/mm)	$K_{exp,av}$ (kN/mm)	$\Delta K_{num/exp}$ (%)
UM	—	—	—	—	—	—	325	243	+34
GTRM	116	142	−18	0.28	0.39	−28	414	365	+13
BTRM	—	—	—	—	—	—	420	553	−24

As for the experimental results, numerical stiffness K_{num} is calculated with P_p and δ_p for UM and BTRM, and with P_k and δ_k for GTRM. The numerical model slightly underestimates both P_k (–18%) and δ_k (–28%). GTRM stiffness is predicted with a good accuracy (error of +13%), although more important deviations are observed for UM and BTRM. However, the values of ΔK provided in Table 14 are compatible with the high dispersion of experimental results that typically characterises these materials (cf. [8]).

Figure 14 shows the numerical load-displacement curves, with a focus on the critical points of damage propagation. UM and GTRM exhibit bed joint sliding between 0.24 and 0.28 mm of vertical displacement (points 1, Figure 14a).

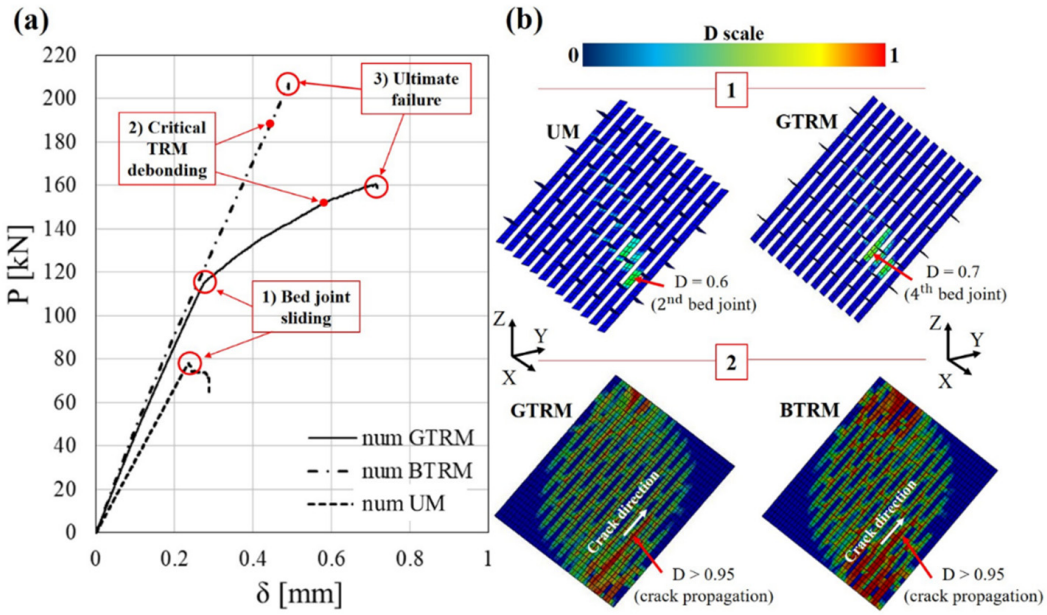

Figure 14. (**a**) Numerical load vs displacement curves; (**b**, part 1) damage distribution in masonry bed and head joints; (**b**, part 2) damage distribution in wall–TRM interface joint.

The reinforcement layer allows GTRM to achieve higher values of D than UM (part 1 of Figure 14b), before the occurrence of sliding. Moreover, as schematised in [15], bed joint sliding is found to produce an abrupt stiffness decrease (knee) in the GTRM curve. Points 2 in Figure 14a identify the initiation of a quick crack propagation in the TRM–wall interface joint due to a critical TRM debonding. Crack position and associated damage D (part 2 of Figure 14b) are approximately the same for GTRM and BTRM. However, BTRM presents higher values of damage than GTRM in the TRM–wall interface joints adjacent to boundary conditions. This is probably the consequence of neglecting damage in the BTRM bed and head joints. For GTRM, the critical bond slippage of the bed joint underneath the propagating crack leads to ultimate failure (point 3, Figure 14a). A critical bed joint sliding at peak load was also observed for the experimental GTRM specimens, as shown in Figure 6c. For BTRM, the ultimate failure (point 3, Figure 14a) is caused by the abrupt propagation of the crack indicated in Figure 14b (part 2, BTRM).

Finally, the proposed simplified micro-model approach allows us to reproduce UM and GTRM experimental damage behaviour quite accurately (cf. Table 7). However, the numerical model is not able to simulate the crack pattern characterising the diagonal traction failure mode of the experimental BTRM. Moreover, the absence of a post-peak softening for the GTRM and BTRM numerical curves is probably due to both the constitutive model and related parameters adopted to describe damage softening in the cohesive elements. In the future, further work is required to explore these latter features.

6. Conclusions

This work proposed the experimental and numerical investigation of masonry panels strengthened with two different commercial TRM techniques. The experimental campaign highlighted how both strengthening systems produce considerable increases in load carrying capacity and stiffness with respect to an unreinforced wall. These results are of crucial importance and make both reinforcing techniques highly suitable for seismic retrofitting of historical masonry in earthquake-prone areas. The different materials and construction methods employed in TRM layer application also affect the damage behaviour and failure modes of the TRM-strengthened masonry. Despite the limited number of tested samples, the experimental results are in agreement with the typical behaviour of single-leaf masonry panels subjected to diagonal compression tests [8,14,15]. GTRM specimens exhibited an initial linear behaviour followed by an abrupt decrease in stiffness (cf. Figure 5) and a subsequent nonlinear response, characterised by TRM debonding. BTRM specimens failed due to diagonal traction without showing intermediate damage. This latter failure mode ensures a more efficient increase and exploitation of the original wall's structural performance. The numerical model was implemented following a simplified micro-model approach. Traditional traction-separation laws were used to describe the constitutive behaviour of interface joints [48,49]. FE simulations showed a good ability to predict experimental results, mostly in terms of macroscopic load-displacement trend (Figure 13), peak loads and stiffness (Tables 13 and 14). The deviations of the numerical results from the experimental ones are compatible with the experimental dispersion typically found in the literature for these materials [8]. Moreover, the numerical model was found to be accurate in reproducing the experimental damage behaviour and failure modes of UM and GTRM with good accuracy. This feature also determines a good prediction capacity for estimating UM and GTRM experimental peak displacements. A theoretical basis for the simulated crack pattern can be found in the experimental literature [15]. For these reasons, the numerical model can be used to explore optimal TRM design options in the future.

Author Contributions: Conceptualization, P.G., A.A., R.R., Y.-H.G. and F.L.; methodology, P.G., A.A., R.R., Y.-H.G. and F.L.; software, P.G., Y.-H.G. and F.L.; validation, P.G., A.A., R.R., Y.-H.G. and F.L.; formal analysis, P.G., A.A., R.R., Y.-H.G. and F.L.; investigation, A.A. and R.R.; resources, A.A.; data curation, P.G., A.A. and R.R.; writing—original draft preparation, P.G.; writing—review and editing, P.G., A.A., R.R., Y.-H.G. and F.L.; visualization, P.G.; supervision, A.A., R.R., Y.-H.G. and F.L.; project administration, A.A., R.R., Y.-H.G. and F.L.; funding acquisition, A.A. and Y.-H.G. All authors have read and agreed to the published version of the manuscript.

Funding: This research received no external funding.

Acknowledgments: LiFE (Laboratori Ingegneria Ferrara) S.r.l., Kerakoll S.p.a and Mucchi Lab, Italy, are acknowledged for offering support during experimental tests. Composite Expertise & Solutions is also gratefully acknowledged for support offered with numerical simulations.

Conflicts of Interest: The authors declare no conflict of interest.

References

1. Basaglia, A.; Aprile, A.; Spacone, E.; Pelà, L. Assessing community resilience, housing recovery and impact of mitigation strategies at the urban scale: A case study after the 2012 Northern Italy Earthquake. *Bull. Earthq. Eng.* **2020**, *18*, 6039–6074. [CrossRef]
2. Grossi, E.; Zerbin, M.; Aprile, A. Advanced techniques for pilotis RC frames seismic retrofit: Performance comparison for a strategic building case study. *Buildings* **2020**, *10*, 149. [CrossRef]

3. Basili, M.; Vestroni, F.; Marcari, G. Brick masonry panels strengthened with textile reinforced mortar: Experimentation and numerical analysis. *Constr. Build. Mater.* **2019**, *227*, 117061. [CrossRef]
4. Bisoffi-Sauve, M.; Morel, S.; Dubois, F. Modelling mixed mode fracture of mortar joints in masonry buildings. *Eng. Struct.* **2019**, *182*, 316–330. [CrossRef]
5. Corradi, M.; Borri, A.; Castori, G.; Sisti, R. Shear strengthening of wall panels through jacketing with cement mortar reinforced by GFRP grids. *Compos. Part B Eng.* **2014**, *64*, 33–42. [CrossRef]
6. Faella, C.; Martinelli, E.; Nigro, E.; Paciello, S. Shear capacity of masonry walls externally strengthened by a cement-based composite material: An experimental campaign. *Constr. Build. Mater.* **2010**, *24*, 84–93. [CrossRef]
7. Gabor, A.; Ferrier, E.; Jacquelin, E.; Hamelin, P. Analysis of the in-plane shear behaviour of FRP reinforced hollow brick masonry walls. *Struct. Eng. Mech.* **2005**, *19*, 237–260. [CrossRef]
8. Garcia-Ramonda, L.; Pelá, L.; Roca, P.; Camata, G. In-plane shear behaviour by diagonal compression testing of brick masonry walls strengthened with basalt and steel textile reinforced mortars. *Constr. Build. Mater.* **2020**, *240*, 117905. [CrossRef]
9. Ismail, N.; Ingham, J.M. In-plane and out-of-plane testing of unreinforced masonry walls strengthened using polymer textile reinforced mortar. *Eng. Struct.* **2016**, *118*, 167–177. [CrossRef]
10. Kouris, L.A.S.; Triantafillou, T.C. State-of-the-art on strengthening of masonry structures with textile reinforced mortar (TRM). *Constr. Build. Mater.* **2018**, *188*, 1221–1233. [CrossRef]
11. Marcari, G.; Basili, M.; Vestroni, F. Experimental investigation of tuff masonry panels reinforced with surface bonded basalt textile-reinforced mortar. *Compos. Part B Eng.* **2017**, *108*, 131–142. [CrossRef]
12. Papanicolaou, C.; Triantafillou, T.; Lekka, M. Externally bonded grids as strengthening and seismic retrofitting materials of masonry panels. *Constr. Build. Mater.* **2011**, *25*, 504–514. [CrossRef]
13. Parisi, F.; Iovinella, I.; Balsamo, A.; Augenti, N.; Prota, A. In-plane behaviour of tuff masonry strengthened with inorganic matrix–grid composites. *Compos. Part B Eng.* **2013**, *45*, 1657–1666. [CrossRef]
14. Shabdin, M.; Zargaran, M.; Attari, N.K.A. Experimental diagonal tension (shear) test of Un-Reinforced Masonry (URM) walls strengthened with textile reinforced mortar (TRM). *Constr. Build. Mater.* **2018**, *164*, 704–715. [CrossRef]
15. Wang, X.; Lam, C.C.; Iu, V.P. Experimental investigation of in-plane shear behaviour of grey clay brick masonry panels strengthened with SRG. *Eng. Struct.* **2018**, *162*, 84–96. [CrossRef]
16. Wang, X.; Lam, C.C.; Iu, V.P. Comparison of different types of TRM composites for strengthening masonry panels. *Constr. Build. Mater.* **2019**, *219*, 184–194. [CrossRef]
17. Wei, C.Q.; Zhou, X.G.; Ye, L.P. Experimental study of masonry walls strengthened with CFRP. *Struct. Eng. Mech.* **2007**, *25*, 675–690. [CrossRef]
18. Yardim, Y.; Lalaj, O. Shear strengthening of unreinforced masonry wall with different fiber reinforced mortar jacketing. *Constr. Build. Mater.* **2016**, *102*, 149–154. [CrossRef]
19. Mininno, G.; Ghiassi, B.; Oliveira, D.V. Modelling of the in-plane and out-of-plane performance of TRM-strengthened masonry walls. *Key Eng. Mater.* **2017**, *747*, 60–68. [CrossRef]
20. Caggegi, C.; Lanoye, E.; Djama, K.; Bassil, A.; Gabor, A. Tensile behaviour of a basalt TRM strengthening system: Influence of mortar and reinforcing textile ratios. *Compos. Part B Eng.* **2017**, *130*, 90–102. [CrossRef]
21. Lignola, G.; Caggegi, C.; Ceroni, F.; De Santis, S.; Krajewski, P.; Lourenço, P.B.; Morganti, M.; Papanicolaou, C.; Pellegrino, C.; Prota, A.; et al. Performance assessment of basalt FRCM for retrofit applications on masonry. *Compos. Part B Eng.* **2017**, *128*, 1–18. [CrossRef]
22. Tomazevic, M. *Earthquake-Resistant Design of Masonry Buildings*; Imperial College Press: London, UK, 1999.
23. Kouris, L.A.S.; Triantafillou, T.C. Design methods for strengthening masonry buildings using textile-reinforced mortar. *J. Compos. Constr.* **2019**, *23*, 04018070. [CrossRef]
24. Bui, L.; Reboul, N.; Si Larbi, A.; Ferrier, E. Mechanical in-plane behaviour of masonry walls reinforced by composite materials: Experimental and analytical approaches. *J. Compos. Mater.* **2017**, *51*, 4231–4249. [CrossRef]
25. Larrinaga, P.; Chastre, C.; Biscaia, H.C.; San-José, J.T. Experimental and numerical modeling of basalt textile reinforced mortar behavior under uniaxial tensile stress. *Mater. Des.* **2014**, *55*, 66–74. [CrossRef]
26. Grande, E.; Imbimbo, M.; Sacco, E. Numerical investigation on the bond behavior of FRCM strengthening systems. *Compos. Part B Eng.* **2018**, *145*, 240–251. [CrossRef]

27. Grande, E.; Milani, G. Interface modeling approach for the study of the bond behavior of FRCM strengthening systems. *Compos. Part B Eng.* **2018**, *141*, 221–233. [CrossRef]
28. Razavizadeh, A.; Ghiassi, B.; Oliveira, D.V. Bond behavior of SRG-strengthened masonry units: Testing and numerical modeling. *Constr. Build. Mater.* **2014**, *64*, 387–397. [CrossRef]
29. Wang, X.; Lam, C.C.; Iu, V.P. Bond behaviour of steel-TRM composites for strengthening masonry elements: Experimental testing and numerical modelling. *Constr. Build. Mater.* **2020**, *253*, 119157. [CrossRef]
30. Wang, X.; Lam, C.C.; Sun, B.C.; Noguchi, T.; Iu, V.P. Effect of curing environment on the tensile behaviour of FRCM composites. *Constr. Build. Mater.* **2020**, *238*, 117729. [CrossRef]
31. Basili, M.; Marcari, G.; Vestroni, F. Nonlinear analysis of masonry panels strengthened with textile reinforced mortar. *Eng. Struct.* **2016**, *113*, 245–258. [CrossRef]
32. De Carvalho Bello, C.B.; Cecchi, A.; Meroi, E.; Oliveira, D.V. Experimental and numerical investigations on the behaviour of masonry walls reinforced with an innovative sisal FRCM system. *Key Eng. Mater.* **2017**, *747*, 190–195. [CrossRef]
33. Garofano, A.; Ceroni, F.; Pecce, M. Modelling of the in-plane behaviour of masonry walls strengthened with polymeric grids embedded in cementitious mortar layers. *Compos. Part B Eng.* **2016**, *85*, 243–258. [CrossRef]
34. Hamdy, G.A.; Kamal, O.A.; El-Hariri, M.O.R.; El-Salakawy, T.S. Nonlinear analysis of contemporary and historic masonry vaulted elements externally strengthened by FRP. *Struct. Eng. Mech.* **2018**, *65*, 611–619. [CrossRef]
35. Wang, X.; Ghiassi, B.; Oliveira, D.V.; Lam, C.C. Modelling the nonlinear behaviour of masonry walls strengthened with textile reinforced mortars. *Eng. Struct.* **2017**, *134*, 11–24. [CrossRef]
36. Gulinelli, P.; Aprile, A.; Rizzoni, R.; Grunevald, Y.H.; Lebon, F.; Lovisetto, R.; Tralli, S. A fe model for TRM reinforced masonry walls with interface effects. *Key Eng. Mater.* **2019**, *817*, 57–64. [CrossRef]
37. Wang, X.; Lam, C.C.; Iu, V.P. Characterization of mechanical behaviour of grey clay brick masonry in China. *Constr. Build. Mater.* **2020**, *262*, 119964. [CrossRef]
38. Pelà, L.; Canella, E.; Aprile, A.; Roca, P. Compression test of masonry core samples extracted from existing brickwork. *Constr. Build. Mater.* **2016**, *119*, 230–240. [CrossRef]
39. Pelà, L.; Roca, P.; Aprile, A. Combined in-situ and laboratory minor destructive testing of historical mortars. *Int. J. Arch. Herit.* **2018**, *12*, 334–349. [CrossRef]
40. *UNI EN 772-1. Methods of Test for Masonry Units—Part 1: Determination of Compressive Strength*; CEN: Brussels, Belgium, 2015.
41. *UNI EN 1015-11. Methods of Test for Mortar for Masonry—Part 11: Determination of Flexural and Compressive Strength of Hardened Mortar*; CEN: Brussels, Belgium, 2007.
42. *EN 1052-1. Methods of Test for Masonry—Part 1: Determination of Compressive Strength; CEN: Brussels, Belgium, 2001.*
43. *UNI EN 1992-1-1. Eurocode 2. Design of Concrete Structures Part 1-1: General Rules and Rules for Buildings*; CEN: Brussels, Belgium, 2005.
44. Galano, L.; Betti, M. *Elementi Di Statica Delle Costruzioni Storiche In Muratura*; Esculapio: Bologna, Italy, 2019.
45. *UNI EN 1052-3. Methods of Test for Masonry Part 3: Determination of Initial Shear Strength*; CEN: Brussels, Belgium, 2007.
46. Ravula, M.B.; Subramaniam, K.V.L. Cohesive-frictional interface fracture behavior in soft-brick masonry: Experimental investigation and theoretical development. *Mater. Struct.* **2019**, *52*, 34. [CrossRef]
47. ASTM International. *ASTM E519. Standard Test Method for Diagonal Tension (Shear) in Masonry Assemblages*; ASTM: West Conshohocken, PA, USA, 2007.
48. Abdulla, K.F.; Cunningham, L.S.; Gillie, M. Simulating masonry wall behaviour using a simplified micro-model approach. *Eng. Struct.* **2017**, *151*, 349–365. [CrossRef]
49. Lourenço Paulo, B.; Rots Jan, G. Multisurface interface model for analysis of masonry structures. *J. Eng. Mech.* **1997**, *123*, 660–668. [CrossRef]
50. Gay, D.; Hoa, S.V.; Tsai, S.W. *Composite Materials: Design and Applications*; CRC Press: Boca Raton, FL, USA, 2002.
51. Thamboo, J.A.; Dhanasekar, M. Nonlinear finite element modelling of high bond thin-layer mortared concrete masonry. *Int. J. Mason. Res. Innov.* **2016**, *1*, 5–26. [CrossRef]
52. Abaqus. *Abaqus 6.13-1*; Dassault Systemes Simulia Corp.: Providence, RI, USA, 2013.
53. Fouchal, F.; Lebon, F.; Titeux, I. Contribution to the modelling of interfaces in masonry construction. *Constr. Build. Mater.* **2009**, *23*, 2428–2441. [CrossRef]

54. Lebon, F.; Dumont, S.; Rizzoni, R.; López-Realpozo, J.C.; Guinovart-Díaz, R.; Rodríguez-Ramos, R.; Bravo-Castillero, J.; Sabina, F.J. Soft and hard anisotropic interface in composite materials. *Compos. Part B Eng.* **2016**, *90*, 58–68. [CrossRef]
55. Rizzoni, R.; Dumont, S.; Lebon, F.; Sacco, E. Higher order model for soft and hard elastic interfaces. *Int. J. Solids Struct.* **2014**, *51*, 4137–4148. [CrossRef]
56. Camanho, P.P.; Dàvila, C.G. *Mixed-Mode Decohesion Finite Elements for the Simulation of Delamination in Composite Materials: NASA/TM-2002–211737*; NASA: Hanover, MD, USA, 2002; pp. 1–37.